SAND2018-1333J

Monitoring Surface Phenomena Created by an Underground Chemical Explosion using Fully-Polarimetric VideoSAR

David A. Yocky, R. Derek West, Robert M. Riley, and Terry M. Calloway

Abstract

Sandia National Laboratories (SNL) flew its Facility for Advanced RF and Algorithm Development (FARAD) X-Band (9.6 GHz center frequency), fully-polarimetric synthetic aperture radar (PolSAR) in VideoSAR-mode to collect complex-valued SAR imagery before, during, and after the sixth Source Physics Experiment's (SPE-6) underground explosion. The VideoSAR products generated from the data sets include "movies" of single and quad polarization coherence maps, magnitude imagery, and polarimetric decompositions. We generated and exploited the VideoSAR image products to characterize the surface effects caused by the underground explosion. Unlike seismic sensors, which measure local area seismic waves using sparse spacing and subterranean positioning, these VideoSAR products captured high-spatial resolution, two-dimensional, time-varying surface movement.

The results from the fifth Source Physics Experiment (SPE-5) used single-polarimetric VideoSAR data. In this paper, we present single-polarimetric and fully-polarimetric VideoSAR results while monitoring the SPE-6 underground chemical explosion. We show that fully-polarimetric VideoSAR imaging provides a unique, coherent, time-varying measure of the surface expression of the SPE-6 underground chemical explosion. We include new surface characterization results from the measured SAR polarimetry (PolSAR) SPE-6 data via polarimetric decompositions and coherent products.

Keywords

Synthetic Aperture Radar (SAR), Autofocus, Coherence, VideoSAR, Polarimetric SAR (PolSAR), Polarimetric Decomposition, Surface Movement, $H/A/\alpha$

I. INTRODUCTION

The Source Physics Experiment (SPE) is part of an ongoing effort by the U.S. Department of Energy, National Nuclear Security Administration (NNSA) to improve its ability to detect, locate, and characterize low-yield underground nuclear explosions (UNEs) anywhere in the world through the analysis of seismic waves [1]. The approach of the SPE is to conduct well-characterized chemical explosions at different depths and in different geologic media and characterize the seismic wave production and propagation from each. Part of this research is modeling the chemical explosion energy transfer and propagation through the geologic media.

The SPE Phase I explosion characterized in this paper was set in a small, Cretaceous granitic intrusive exposed at land surface with relatively thin Paleozoic sedimentary rocks, rhyolitic Miocene volcanic rocks, and Cenozoic alluvium occurring along the flanks of the intrusive. The sixth SPE explosion (SPE-6) at the SPE Phase I site had a burial depth of 31.4 meters with a TNT equivalent yield of 2245 kg. Figure 1(a) shows a Google Earth© image of the SPE pad.

A. Seismic Sensors

The SPE phase I site is instrumented with seismic sensors. One example is five geophone lines that radiate outward up to 20 kilometers from the SPE source hole. The lines cross a variety of geologic and topographic regimes. Seismic waves generated by SPE-series of explosions propagate outward from the detonation point through the three-dimensional (3-D) geological structure of the earth. Geophone lines are part of a larger effort to integrate the known geologic complexity of the area via 3-D geological framework models of the area with SPE-related seismic wave analyses.

B. Synthetic Aperture Radar

Synthetic aperture radar (SAR) is a side-looking, remote sensing radar operating in the microwave region of the electo-magnetic (EM) spectrum that can create high-resolution imagery through coherent signal processing techniques [2]. The radar sensor is both the illuminator/transmitter and receiver and is independent of solar illumination allowing day/night imaging. In some regions of the EM spectrum, SAR avoids effects of clouds, fog, rain, smoke and dust.

VideoSAR is a circle-mode collection of a target [3] with the SAR spot-lighted on the center of the scene. Received pulses are a continuous interrogation of the scene as the airplane flies a circle. Therefore, the target is interrogated from a single elevation (grazing) angle and every aspect angle, but more important for this experiment, it captures the explosion without detailed synchronization with the detonation timing. Multiple circles were flown and data were collected, before, during, and after the explosion with the same imaging geometry. Using VideoSAR coherent processing during an explosion should provide time-varying, two-dimensional surface change products that can be compared to seismic and other surface/contact sensors that were deployed for the event. The area imaged by the SAR sensor is shown in a vertical-polarization transmitted, vertical-polarization received (VV), 0.125-meter square pixel, ground-plane geomapped [4] magnitude SAR image in figure 1(b).

C. SAR Imaging Assumptions

SAR imaging assumes the imaged scene consists of static radar scatterers. Yet, during the explosion surface expression may be dynamic and small dirt particles may be ejected into the air creating a dust plume. The SAR radiation should be able to penetrate this and monitor the surface. When a scatterer is moving during the SAR collection aperture, the focus and position of the scatterer can change in the final image. Therefore, SAR imaging of an explosion may present blurred targets if the energy from the explosion displaces ground and other surface objects. Motion-like de-focus may also be present if scatterers vibrate.

Additional observables afforded by SAR surface monitoring include time-varying surface coherence change and fully-polarimetric SAR (PolSAR) measures. Derived surface properties, such as spatially- and time-varying scattering mechanisms and degree of coherence before, during and after the explosive event provide information on how energy propagated and interacted with the surface.

D. Previous Results

The fifth SPE explosion (SPE-5) at the SPE Phase I site had a burial depth of 76.5 meters with a TNT equivalent yield of 5035 kg. SAR data, with VV polarization, were collected in VideoSAR circle-mode of the SPE-5 chemical explosion event with the SAR spot-lighted on the center of the scene and were processed to create imagery of the scene. Coherent processing products consisting of coherent change detection (CCD) maps, phase difference maps, DEMs, and differential DEMs were also produced. The VideoSAR continuous target interrogation allowed high-precision matching of the coherent apertures for product generation to monitor the surface change characteristics [5].

Dynamic coherence showed that the SPE pad surface scatterers moved in time and created a permanent reduction in coherence. More importantly, portions of the SPE pad lost coherence and then regained coherence, which was indicative of a transient elastic deformation during the explosion.

II. SAR DATA COLLECTION

Sandia National Laboratories (SNL) flew its Facility for Advanced RF and Algorithm Development (FARAD) X-Band, 9.6 GHz center frequency, fully-polarimetric synthetic aperture radar (SAR) on a DeHavilland Twin Otter (DHC-6) over the SPE pad located on the Nevada National Security Site on October 12, 2016 for the SPE-6 explosion. The airborne SAR flew at 3.5 km slant range, grazing angle of 38.3-degrees, and approximately 2185 m above scene local ground altitude. The X-band FARAD SAR transmitted a 1.36 GHz bandwidth chirped signal. The DHC-6 flew two full-circle passes before SPE-6 chemical explosion, a full circle during which the explosion occurred, and then two more full circles after the explosion event, collecting imagery in spotlight, circle-mode. Two passes pre- and post-event allow for coherent processing and the generation of coherent image products, such as coherence change detection (CCD) maps.

III. SAR SIGNAL PROCESSING

A. *Image Formation*

VideoSAR-mode SAR images were produced using the polar format algorithm [2] with a Taylor window aperture weighting function, with parameters side-lobe level (SLL) = -40 dB and $\bar{n}$ = 10. Continuously collected phase history allows selectable azimuth time spacing between images to create a frame rate. The azimuth sample interval for the collections was nominally 800 Hz. Ground plane range resolution was nominally 0.125 meters. Approximately 6000 azimuth samples, or 8 seconds of synthetic aperture were needed to obtain 0.125-meter azimuth resolution. Shorter apertures can be used to resolve phenomenology on a finer time scale [5], at the expense of spatial resolution. We explored azimuth resolutions from 0.125 meter to 2 meter, or from approximately an eight-second aperture to approximately a 0.5-second aperture, respectively. After images were formed, they underwent spatially varying-autofocus to account for uncompensated motion of the SAR sensor. The spatially-varying autofocus is a new approach developed for this application and is discussed in the next section. A variety of coherent single-polarization and SAR polarimetric (PolSAR) products were then produced. Each image was used as a frame for the VideoSAR movie. The time between frames were either 0.1 second, or 0.05 second, depending on the frame rate desired. This produced a movie of images as the airplane flew a circle around the SPE explosion events.

B. Autofocus

For spotlight-mode collections where the SAR platform does not follow a straight flight path, phase-history data are collected on a non-planar ribbon in three-dimensional Fourier space. The polar format algorithm expects data collected on a plane in Fourier space. The non-planar ribbon induces phase errors which blur the image. Scatterers that lie in the focal plane of the image are focused while those outside of the focal plane are defocused, creating a depth-of-focus issue. Given a circular collect and terrain height variation in the scene, scatterers on the pad are focused while those upslope on the mountain become increasingly defocused in cross-range as can be seen in figures 2(a) and 2(b). The phase error injected into the image on a pulse-by-pulse basis is given by

$$\Delta\phi = \frac{4\pi\Delta z_{max}}{\lambda R_o} \tag{1}$$

where λ is the center-frequency wavelength, R_o is the slant range, and Δz_{max} is the maximum out-of-slant-plane distance that occurs over the aperture. The shape of the phase error over the aperture is proportional to the shape of the out-of-plane motion. For a circle collection, the shape of this phase is approximately quadratic. Any quadratic phase error that exceeds $\pm\pi/4$ radians produces significant widening of a point scatterer [2]. Using this metric, the depth-of-focus (DOF) is computed as

$$DOF = \frac{\lambda R_o}{16\Delta z_{max}}. \tag{2}$$

The focal plane of each image passes through the scene reference point, which is the explosion source-hole coordinates and height. At the SPE pad, a hill rises immediately to the west north-west to a height of approximately 10 meters above the focal plane. The DOF is 1.0 meter or less for most apertures in the VideoSAR collects over SPE. Therefore, targets with heights within 1.0 meter of the scene center height are focused well, and those with heights greater than 1.0 meter of scene center height are defocused proportionately with the height difference compared to scene center.

C. Phase Gradient Autofocus

Phase gradient autofocus (PGA) is a non-parametric approach to correcting phase errors in a SAR image [6]. It takes advantage of the redundancy of the phase-error function by averaging across many range cells, and the phase-error function is derived using a maximum-likelihood estimation. Taking measurements of the phase difference for a given aperture position and summing them as a function of position, produces a data-driven phase error estimate that then can be removed from the image.

Figure 2(a) shows a zoomed-in portion of a VV-polarization geo-mapped SAR magnitude image of the SPE pad area that has PGA applied. Note there is still defocus because of the small depth of focus and the large elevation variation across the scene. Figure 2(b) shows a zoom of some of the defocused targets to the west-northwest of the experiment pad.

D. Digital Elevation Autofocus

Globally-applied PGA [6] fails to focus all targets in the VideoSAR imagery of SPE-6 because of the circular collection geometry, additional airplane out-of-plane motion, and scene height variations. Therefore, for this explosion monitoring experiment, we developed a spatially-varying autofocus algorithm based on an input DEM. A high resolution LIDAR DEM [5] of the SPE site was used as the DEM. This step is necessary to achieve better focusing throughout the images, and thus, better registered coherent targets. Since the same DEM is used for all images, the focusing is the same for all images within a polarimetric SAR image set and no phase difference is introduced between the polarimetric channels.

As described above, the out-of-plane motion of the SAR through the imaging aperture creates target defocus for targets with heights greater than the depth-of-focus metric in (2). The SAR sensor position is well known and deviation from a straight-line collection can be calculated. The long aperture needed to create the 0.125-meter ground-plane resolution combined with the relatively short range from the sensor to scene center can exacerbate the out-of-plane defocusing effects.

For the VideoSAR collections reported here, the major contribution to the defocus is a quadratic function. Therefore, the quadratic out-of-plane motion is calculated utilizing (2). Using the LIDAR DEM resampled to the SAR image resolution, the quadratic phase error is scaled to the relative height above or below the scene reference point height, and removed.

Figure 2(c) shows a zoomed portion of the original test site after the digital elevation autofocus quadratic phase compensation is applied. Compared to figure 2(b), point reflector main-lobe supports are tighter. After the digital elevation autofocus, higher-order phase-error can be removed using conventional PGA. This was not needed for the SPE-6 VideoSAR data.

IV. SINGLE-POLARIZATION SAR PRODUCTS

A. Imagery

Images were formed from the measured data with square 0.125-meter resolution cells and were focused using the digital elevation autofocus described previously. The images were then geo-located into a latitude-longitude grid. Frames for the movies were twofold: 0.1 and 0.05 seconds apart. Figure 1(b) shows a full SAR magnitude image of the SPE area. Figure 3 shows a series of frames from the VideoSAR movie capturing the SPE-6 explosion event. These are VV polarization images that are 0.0 second, 2.0 seconds and 4.5 seconds, after the explosion according to the time of the middle pulse of the image. On close inspection, there may be small magnitude changes from before and after the chemical explosion on the graded portions of the experimental pad, but this magnitude change is subtle.

B. Coherence

The complex correlation coefficient was calculated using co-registered complex-valued images from the passes before and during the explosion event,

$$\gamma_{CCD} = \frac{\sum_{k=1}^{N} X_{1,k}^{*} X_{2,k}}{\sqrt{\sum_{k=1}^{N} |X_{1,k}|^2 \sum_{k=1}^{N} |X_{2,k}|^2}}, \tag{3}$$

where $X_{1,k}$ and $X_{2,k}$ represent the k^{th} complex values of the co-registered images from passes 1 and 2 respectively, and the $*$ symbol denotes the complex conjugate operation. The summation in (3) occurs over a neighborhood (also called a ”box” or ”window”) of image samples, with N representing the number of samples in the window (generally known as the ”number of looks”). A 5×5 ensemble box size was used in our coherence product generation and the coherence maps were geo-mapped into a latitude/longitude grid.

The magnitude of (3), $|\gamma_{CCD}|$, gives the so-called the degree of coherence [7], [8] and the angle gives a phase-wrapped interferogram that can be unwrapped to give the topography of the scene [2], [9], [10], [11]. Height maps from before the explosion and after the explosion could be compared to give the relative height change, [12], [13]; this research objective is not explored in this paper.

Sample frames from the VideoSAR coherence movie are shown in figure 4. These are the same frames as shown in figure 3 with a wider area presented so that the coherence change around the experiment pad can be seen. The grayscale products in the sub-figures show the degree of coherence; high coherence is white and no coherence, sometimes called decorrelation, is black. The degrees of coherence are represented as gray-levels in a continuum of coherence from 0 (no coherence) to 1 (high coherence). Figure 4(a) shows the coherence of the scene just before the SPE-6 explosion. Note that most of the coherence is white or light gray. Low coherence areas are mostly shadows created by the muck pond (the area to catch the drilling debris), the experiment shed, rocks on the left-side of the pad, and from sparse vegetation. Vegetation typically measures as lower-coherence due to volume scattering. Figure 4(b) is the coherence product 2 seconds after the explosion. Note the increased decorrelation to the left of the pad, which is up a hill, decorrelation down the sides of the pad to the muck pond, and a mottled correlation/decorrelation on a line traveling northeast (lower left corner to upper right corner) through the pad. Figure 4(c) shows the site coherence 4.5 seconds after the explosion. Note that coherence near the muck pond has increased. Other portions of the site, the hillside, the edges to the muck pond, and edges around the utility roads stay decorrelated.

What causes the loss in coherence? Coherence is a magnitude and phase measure of the SAR clutter similarity. High coherence (white in the coherence products) means the ground reflectors and their phases appear alike at the collection geometry and over the time lapse between the two complex-valued SAR images. Low coherence can occur due to low returns from the ground scatterers and from volume scattering from vegetation. In the case of explosive energy being transferred and propagated through the ground, the drop in coherence can be from surface disturbance. The ground scatterers can be displaced and re-oriented with respect to the SAR sensor, and physically being lifted and landing in a different orientation. The associated geophysical phenomenology is referred to as spallation. Spallation corresponds to movement of surface material due to impact, shock of an explosion , or stress - including internal stress of rocks that leads to fractures. In this process, fragments of the original material are moved or ejected from their original position due to impact, explosion, or stress. It also means rock breaking off a rock face due to internal stresses. Spallation and surface disturbance can explain coherence loss that stays decorrelated as a function of time. Surface disturbance does not explain the surface phenomenology where the surface coherence drops and then coheres again as a function of time.

The coherence near the muck pond varies from coherent to incoherent in time. This suggests an elastic deformation process where the pad surface is moved physically causing the ground reflectors reduction in coherence, perhaps by changing its geometry to the SAR sensor as a function of time, but partially restoring the original geometry after the explosive energy dissipates. The coherence could also drop due to energy being injected into the scene.

The high spatial resolution imagery presented thus far exploits pulses gathered for approximately 8 seconds. Therefore, the pulses capturing the explosion can produce decorrelating magnitude and phase in the video frame coherence measures for about 8 seconds. This provides motivation to examine smaller aperture image-integration times to refine the surface expression's time duration.

VideoSAR complex-valued imagery was formed with 2.0-m azimuth resolution, and full-range spatial resolution, 0.125 meters. The azimuth resolution results from a 0.50 second synthetic aperture. Frames from the VideoSAR were created using a 0.05 second interval increment between VideoSAR apertures. Complex-valued image frames from the same geometries before the explosion and during the explosion were registered and the resulting coherence products were examined. With increased temporal resolution, it was determined that it took approximately 0.5 seconds for the energy from the explosion to dissipate. Figure 5 shows geo-mapped coherence from (a) just before the explosion, (b) 0.10 seconds into the explosion, (c) 0.25 seconds into the explosion, and (d) 0.50 seconds after the explosion. The physical explosive is 31.4 meters below the pad, and the pad is approximately 100 meters in length. The time from before the explosion to pad decorrelation provides an estimate of the energy speed in the SPE pad media. The speed calculated is approximately 314 m/s, which agrees with the p-wave velocity of 300 m/s to 500 m/s measured in the SPE pad weathered granite.

Another way of visualizing the coherence change is to monitor selected parts of the image, documenting how they change as a function of time. With this approach we monitored three areas of interest in VideoSAR complex images that were formed with a .3048-m azimuth resolution and full-range spatial resolution, 0.125 meters. Figure 6(a) shows the geo-mapped magnitude imagery before the explosion with the three areas of interest: the blue box is close to ground zero, the green box is in the muck pond at a lower elevation that the experimental pad, and the red box is away from ground zero in desert scrub. Figure 6(b) shows the coherence change as a function of time for the three different locations described above: the blue plot is the box close to ground zero which decorrelates as a function of the explosive energy disturbing the earth, the green plot is the muck pond which initially decorrelates then rebounds in coherence, and the red plot is the desert scrub and stays correlated throughout the explosion.

C. Complex Reflectance Change Detection

SAR coherence is known to be low where in areas of low clutter-to-noise ratio (CNR), even if the region has not changed between SAR collections. The maximum-likelihood change estimate, called the complex reflectance change detection (CRCD) or maximum-likelihood coherent change detection (MLCCD), takes into account the CNR levels of the SAR images to discern between changes in the scene that may have occurred between the two SAR collections and low CNR regions [14]. MLCCD and CRCD are change detection methods, not a measures of coherence. The CRCD and MLCCD are equivalent and are given by

$$\gamma_{MLE} = \frac{\left|\sum_{k=1}^{N} X_{1,k}^{*} X_{2,k}\right|}{\sum_{k=1}^{N} \left|X_{1,k}\right|^{2} + \sum_{k=1}^{N} \left|X_{2,k}\right|^{2} - N\sigma_{n1}^{2} - N\sigma_{n2}^{2}} \tag{4}$$

where the same notation in (3) applies here with the addition of σ_{n1} and σ_{n2}, which represent the system thermal noise variance in the images from passes 1 and 2, respectively. Figure 7 compares (a) the coherence versus (b) the MLCCD product before the explosive event. Note that the MLCCD increases the coherence for the low-return roads and shadows, denoting these areas as white in the correlation map, which represents no change. Figure 8(a) shows the coherence and figure 8(b) the MLCCD after the SPE-6 explosion event. Once again, the roads that have a loss of coherence due to low clutter-to-noise levels are corrected to high values in figure 8(b) leaving the loss of coherence due to surface change and spallation.

V. FULLY-POLARIMETRIC VIDEOSAR MEASURES

The SNL X-Band FARAD fully-polarimetric SAR transmits orthogonal vertical and horizontal, linearly-polarized pulses in a multiplexed scheme. A frequency-modulated, horizontally-polarized pulse is transmitted and the complex-valued reflectance is received on both the horizontal and vertical polarization channels. Then a frequency-modulated, vertically polarized pulse is transmitted and the complex-valued reflectance is again received on both horizontal and vertical polarization channels. The co- and cross-polarization channels measure the complete scattering matrix of the scene at a given incidence angle [15].

To discern meaningful information from polarimetric SAR (PolSAR) measurements, the received data needs to be calibrated. Calibration consists of compensating for the effective antenna patterns (magnitude and phase) of the different polarization channels, accounting for the differential phase that occurs from multiplexing the pulses, and radiometric calibration which balances the polarimetric channels and converts to units of radar cross-section (RCS) in the images.

PolSAR image sets that have been properly calibrated can be processed through so-called polarimetric decomposition algorithms, which provide parameters that convey elementary scattering-physics of the scatterers within the scene. For example, the general four-component scattering power decomposition (G4U) algorithm provides surface, dihedral, volumetric, and helical scattering powers [16]. A more recent contribution to polarimetric decompositions is the model-based Dauphin decomposition that minimizes residual error by generalizing a parameter [17]. The polarimetric decomposition that we will use through the remainder of this paper is the information-theoretic $H/A/\alpha$ decomposition [18].

The chemical explosion may change the nature of some of the surface polarization responses. Creating different polarimetric decomposition products may show new aspects of surface disturbance and provide insight into surface phenomenology compared to the single-channel results above. Moreover, products generated from full-polarization coherent processing may produce additional information about the explosion and its influence on the surface scatterers.

A. H/A/α Decomposition

In 1997, Cloude and Pottier proposed the information-theoretic $H/A/\alpha$ unsupervised classification scheme based on the use of the entropy (H), anisotropy (A), and a roll-invariant scattering-mechanism parameter (α) [18]. The idea is that entropy arises as a natural measure of the inherent reversibility of the scattering surface, and the α angle can be used to identify the underlying average scattering mechanisms.

The $H/A/\alpha$ decomposition parameters are found from the PolSAR measurements as follows. The complex-valued image data formed from the different polarization channels can be combined into the so-called Pauli feature vector,

$$\mathbf{k}_p = \frac{1}{\sqrt{2}} \begin{bmatrix} S_{HH} + S_{VV} \\ S_{HH} - S_{VV} \\ 2S_{HV} \end{bmatrix} . \tag{5}$$

where S_{ik} are the components of the coherent Sinclair matrix with the convention of scattered (received) polarization as the first subscripted letter and incident (transmitted) polarization the second subscript. The first element of the Pauli feature vector emphasizes scattering mechanisms in the scene that have an odd number of reflections, such as surfaces. The second element emphasizes scatterers that have an even number of reflections, such as a vertically or horizontally oriented dihedral. The last element emphasizes responses from dihedral scatterers rotated to an angle of $45°$.

The Pauli feature vector is formed for every pixel in a PolSAR image set. A spatial average of the outer-product of the Pauli feature vector, in a local neighborhood of each pixel, creates the so-called coherency matrix,

$$T = \left\langle \mathbf{k}_p \mathbf{k}_p^\dagger \right\rangle = \begin{bmatrix} T_{11} & T_{12} & T_{13} \\ T_{21} & T_{22} & T_{23} \\ T_{31} & T_{32} & T_{33} \end{bmatrix}, \tag{6}$$

where the notation $\langle \cdot \rangle$ indicates a spatial average and † denotes a conjugate-transpose. Because of their construction, the coherency matrices are positive semi-definite.

The $H/A/\alpha$ decomposition computes an eigen-decomposition on each of the coherency matrices. Since the coherency matrices are positive semi-definite, the eigenvalues are real and non-negative. Assume the eigenvalues are ordered as $0 \leq \lambda_3 \leq \lambda_2 \leq \lambda_1$. Pseudo-probabilities can be computed from the eigenvalues as follows,

$$P_i = \frac{\lambda_i}{\sum_{n=1}^{3} \lambda_n}. \tag{7}$$

The entropy parameter, H, is computed from the pseudo-probabilities,

$$H = -\sum_{i=1}^{3} P_i \log_3 P_i. \tag{8}$$

The anisotropy parameter, A, is measures the relative strength of the second and third eigenvalues and is computed as,

$$A = \frac{\lambda_2 - \lambda_3}{\lambda_2 + \lambda_3}. \tag{9}$$

Finally, the first element of each of the three eigenvectors is modeled as,

$$\mathbf{e}_i(1) = e^{j\phi_i} \cos \alpha_i; \tag{10}$$

the roll-invariant scattering parameter, α is computed as the weighted average of the α_i values,

$$\alpha = \sum_{i=1}^{3} P_i \alpha_i. \tag{11}$$

Figure 9 illustrates the scene in passes (a) before the explosion, (b) during the explosion, and (c) after the explosion. Notice that there is a change of hue on the pad before the explosion and after; analysis of the H and α decomposition parameters help to understand how the surface has changed due to the explosion.

The soil on the surface of the pad is disturbed and loosened during the explosion, which changes the measured response in the $H/A/\alpha$ parameter space. To illustrate this, a 256×256 chip was extracted from the pad and the $H/A/\alpha$ parameters were computed for 180 VideoSAR frames (18 seconds) surrounding the explosion. The VideoSAR frames are separated by 0.1 seconds and the explosion takes place at frame 40, or at 4.0 seconds. The centroids of the H/α values computed within each chip are plotted in figure 10 and illustrate that there is a migration of the parameters in the H/α plane due to the explosion. Furthermore, to gain a sense of the change of the shape of the distribution in the H/α plane, a 2-D histogram of the H/α values was computed from the data in each chip and the contours were found that contained approximately half of the H/α histogram counts around the mode. The contours for frames 1, 56, and 180, corresponding to times 0.0, 5.6, and 18.0 seconds, are also plotted in figure 10 to show how the distribution changes before, during, and immediately after the explosion. To further understand the progression of the distribution of H/α values, the area of each of the 180 contours was found and is displayed in figure 11. It is clear that before the explosion the areas of the contours are close the contour areas from the pass before the explosion; furthermore, it is readily seen that the explosion takes place at around frame 40, which corresponds to 4.0 seconds. According to the peak in figure 11, however, it takes about 1.6 seconds for the VideoSAR aperture to contain enough measured phase history samples to show the full response. Note that H/α values and contours do not migrate back to pre-explosion values or positions in the H/α plane.

B. Optimum Coherence

Optimum coherence from polarimetric SAR coherent processing considers the linear combination of polarization states that yield the highest coherence. This approach attempts to increase coherence using all of the polarimetric channels leaving only true change or low clutter-to-noise areas with low coherence. The Pauli feature vectors given in (5) from a co-registered PolSAR image sets, from two temporally-separated passes, can be stacked into a six-element vector and a 6×6 coherency matrix can then be computed:

$$T_6 = \begin{bmatrix} \left\langle \mathbf{k}_1 \mathbf{k}_1^\dagger \right\rangle & \left\langle \mathbf{k}_1 \mathbf{k}_2^\dagger \right\rangle \\ \left\langle \mathbf{k}_2 \mathbf{k}_1^\dagger \right\rangle & \left\langle \mathbf{k}_2 \mathbf{k}_2^\dagger \right\rangle \end{bmatrix} = \begin{bmatrix} T_1 & \Omega_{12} \\ \Omega_{12}^\dagger & T_2 \end{bmatrix} \tag{12}$$

where T_1 and T_2 are the 3×3 coherency matrices computed from passes 1 and 2, and Ω_{12} is the 3×3 cross-coherency matrix.

The so-called optimum-coherence formulation computes an estimate of the coherence from the equation [19], [15],

$$\gamma_{Opt} = \frac{\mathbf{w}_1^\dagger \Omega_{12} \mathbf{w}_2}{\sqrt{\left(\mathbf{w}_1^\dagger T_1 \mathbf{w}_1\right)\left(\mathbf{w}_2^\dagger T_2 \mathbf{w}_2\right)}}, \tag{13}$$

by determining the complex-valued weighting vectors $\mathbf{w}_1$ and $\mathbf{w}_2$ that maximize the coherence. All of the quantities in (13) can be computed from the data, except for the weighting vectors, which are found by casting (13) as optimizing a Lagrange equation,

$$\begin{aligned} L\left(\mathbf{w}_1, \mathbf{w}_2\right) &= \mathbf{w}_1^\dagger \Omega_{12} \mathbf{w}_2 + \mu_1 \left(\mathbf{w}_1^\dagger T_1 \mathbf{w}_1 - C_1\right) \\ &\quad + \mu_2 \left(\mathbf{w}_2^\dagger T_2 \mathbf{w}_2 - C_2\right). \end{aligned} \tag{14}$$

Computing the gradients and solving for the weighting vectors gives the following coupledeigenvalue equation,

$$T_2^{-1}\Omega_{12}^{\dagger}T_1^{-1}\Omega_{12}\mathbf{w}_2 = \nu\mathbf{w}_2 \tag{15}$$

$$T_1^{-1}\Omega_{12}T_2^{-1}\Omega_{12}^{\dagger}\mathbf{w}_1 = \nu\mathbf{w}_1. \tag{16}$$

The optimal weighting vectors are the eigenvectors associated with the largest eigenvalue.

The magnitude of (13), $|\gamma_{Opt}|$, gives the optimum coherence and the angle gives the associated phased-wrapped interferogram that can also be unwrapped to give the topography of the scene. Optimum coherence maps of the scene are illustrated in figures 12(a) before the explosion and 12(b) after the explosion. The important thing to note from the optimum coherence map is that the maximum coherence is found across linear combinations of the polarimetric channels and a loss of coherence indicates that the area may have low CNR or that a change has occurred (coherence could not be found across all polarimetric channels).

C. Multi-Polarization Change Detection

The coherence map, computed from a single-polarization channel, illustrated low coherence due to disturbances in surface scatterers. In a similar manner, a polarimetric change detection method for detecting changes over time was developed by Novak [20]. The maximum likelihood polarimetric change detection is given by

$$\gamma_{Nov} = \frac{\sum_{k=1}^{N}\left(\mathbf{x}_k^{\dagger}C^{-1}\mathbf{y}_k e^{j\phi} + \mathbf{y}_k^{\dagger}C^{-1}\mathbf{x}_k e^{-j\phi}\right)}{\sum_{k=1}^{N}\left(\mathbf{x}_k^{\dagger}C^{-1}\mathbf{x}_k + \mathbf{y}_k^{\dagger}C^{-1}\mathbf{y}_k\right)}, \tag{17}$$

where

$$\mathbf{x} = \begin{bmatrix} HH \\ HV \\ VV \end{bmatrix}, \quad \mathbf{y} = \begin{bmatrix} HH \\ HV \\ VV \end{bmatrix} \tag{18}$$

are the fully-polarimetric data sensed at two different times with the same transmit and receive conventions as above, and the matrix C^{-1} is the inverse of the covariance matrix of the measurements, $C = E\left\{\mathbf{x}\mathbf{x}^\dagger\right\}$ (it is assumed that $\mathbf{x}$ and $\mathbf{y}$ have the same covariance structure). If polarization whitening is applied to the SAR data such that

$$\begin{aligned} \tilde{\mathbf{x}}_k &= C^{-1/2}\mathbf{x}_k && (19) \\ \tilde{\mathbf{y}}_k &= C^{-1/2}\mathbf{y}_k, && (20) \end{aligned}$$

then after some algebraic manipulation, (17) is the maximum likelihood change given by

$$\tilde{\gamma}_{Nov} = \frac{2\left|\sum_{k=1}^{N} \tilde{\mathbf{x}}_k^\dagger \tilde{\mathbf{y}}_k\right|}{\sum_{k=1}^{N} ||\tilde{\mathbf{x}_k}||^2 + \sum_{k=1}^{N} ||\tilde{\mathbf{y}_k}||^2}. \tag{21}$$

This equation is applied to the fully-polarimetric data for monitoring the SPE-6 underground explosion and is shown in figure 13(a). Comparing figure 13(a) with figure 8(a), more degrees of decorrelation are apparent from the PolSAR maximum likelihood change detection than the single-polarization coherence measure. There is an apparent drop of the total coherence when compared to the single polarization coherence. This decrease in total full-polarimetric coherence may be because of increased sensitivity in one or more of the polarimetric channel combinations.

D. Multi-Polarization Change Detection with Noise

Equation (21) provides polarimetric maximum likelihood change detection, but does not take into account the system noise, as does the single-channeled complex reflectance change detection in (4). Let $\mathbf{x}$ and $\mathbf{y}$ be defined as

$$\mathbf{x} = \begin{bmatrix} HH_1 \\ HV_1 \\ VV_1 \end{bmatrix} + \begin{bmatrix} \eta_{HH} \\ \eta_{HV} \\ \eta_{VV} \end{bmatrix} = \begin{bmatrix} HH_1 \\ HV_1 \\ VV_1 \end{bmatrix} + \boldsymbol{\eta} \tag{22}$$

$$\mathbf{y} = \begin{bmatrix} HH_2 \\ HV_2 \\ VV_2 \end{bmatrix} + \boldsymbol{\eta}, \tag{23}$$

where subscripts 1 and 2 denote the different passes and where the noise vector, $\boldsymbol{\eta}$, has covariance matrix

$$\Sigma = E\left\{\boldsymbol{\eta}\boldsymbol{\eta}^{\dagger}\right\} = \begin{bmatrix} \sigma_{HH}^2 & 0 & 0 \\ 0 & \sigma_{HV}^2 & 0 \\ 0 & 0 & \sigma_{VV}^2 \end{bmatrix} \tag{24}$$

and models the system thermal noise contribution. With this definition, both the signal and noise will be whitened in Novaks multi-polarization change detection approach. The whitened noise variance can be subtracted from the signal power, as in the single-channel complex reflectance change detection in (4), so that (21) becomes

$$\tilde{\gamma}_{NovMLE} = \frac{2\left|\sum_{k=1}^{N} \tilde{\mathbf{x}}_k^{\dagger}\tilde{\mathbf{y}}_k\right|}{\sum_{k=1}^{N} ||\tilde{\mathbf{x}_k}||^2 + \sum_{k=1}^{N} ||\tilde{\mathbf{y}_k}||^2 - N\sigma_{\tilde{\mathbf{x}}}^2 - N\sigma_{\tilde{\mathbf{y}}}^2}, \tag{25}$$

where the noise variance $\sigma_{\tilde{\mathbf{x}}}^2 = \mathrm{Trace}\left(\Sigma C^{-1}\right)$, similarly for $\sigma_{\tilde{\mathbf{y}}}^2$. Subtracting the whitened system noise gives a change detection that compensates for the noise levels of the polarimetric channels. The result of this approach is shown in figure 13(b) for an image set after the explosion. Note that the overall change in figure 13(b) is greater than figure 13(a). Some of the shadows in the boulders on the slope away from the experiment ground zero are filled with no change due to high noise-to-clutter in those areas. This result is similar to the result found by the MLCCD approach for single polarization channels shown in figure 8(b). Figure 13(b) shows that the fully-polarimetric change detection with noise compensation, is superior in correcting low CNR decorrelations on roads and in shadows than the single polarization MLCCD results in figure 8(b) showing the added information and value of PolSAR coherent products for monitoring surface disturbances.

E. Doppler Detection

As mentioned in the introduction, a SAR sensor collects measurements of a scene by sequentially transmitting and receiving pulses. There is an underlying assumption that the scatterers in the scene are stationary during the data acquisition process; if they aren't, then the energy received from them will not properly focus during the image formation process and will leave a distinctive Doppler-induced blur in the final image. This is seen by the Doppler frequency f_d imparted by a moving target with change in range, $\dot{R}$, of

$$f_d = -\frac{2\dot{R}f_o}{c} = -\frac{2\dot{R}}{\lambda} \tag{26}$$

where λ is the wavelength corresponding to the SAR waveform center frequency f_o and $\dot{R}$ is

$$\dot{R} = v_R + a_R t \tag{27}$$

for a moving target, with v_R the velocity and a_R the acceleration that is changing range, R [21].

For a vibrating target, $\dot{R}$ becomes

$$\dot{R} = D_v \omega_v \left(t\right) \tag{28}$$

with D_v denoting the maximum vibrational displacement and $\omega\left(t\right)$ the angular frequency as a function of time [22].

The VideoSAR data collected from the scatterers in the scene follow the stationarity assumption until the explosion occurs. After the SPE-6 explosion, the chemical explosion energy propagates to the surface, and disturbs the soil near ground-zero as shown in the preceding results. Furthermore, the transient energy may impart motion to targets, including ejecta, and vibrations, influencing vegetation and rocks in the scene. The vibrational formulation of Doppler smear in (28) is applicable to vibrations induced by an underground chemical explosion. After the explosive energy dissipates, the scatterers in the scene should eventually become stationary again.

With polarimetric image sets, combinations of the images formed from different channels highlight different types of Doppler energy. We processed different combinations of the images within the PolSAR image sets through a tuned-Doppler detector to capture the Doppler signatures from the various scatterers in motion. As a baseline for comparison, the images formed from each polarization channel were processed through the Doppler detector. The Doppler detections from the co-polarization images and cross-polarization images are displayed in figures 14(a) and 14(b), respectively. It can be seen that the VV co-polarization channel tends to detect more on the rocks and vegetation. In contrast, the HH co-polarization channel detects more of the disturbed soil on the pad, with some detections on the rocks and vegetation. The cross-polarization channels detect mostly on the soil on the pad with a few detections on the surrounding rocks and vegetation. The different polarization channels can be coherently combined to emphasize rudimentary scattering physics, for example, summing the co-polarization channels emphasizes odd-bounce scattering mechanisms such as surfaces. The Doppler detections from the sum and difference of the co-polarization images and cross-polarization images are displayed in figures 15(a) and 15(b), respectively.

The plots in figures 14 and 15 illustrate the spatial distribution of the Doppler detections, but do not convey the temporal distribution of the detections from the VideoSAR images. The plots in figure 16 illustrate the number of Doppler detections found in each VideoSAR frame for the co- and cross-polarization images and the coherent sums and differences of the co- and cross-polarization images. From the figure, it is clear that the temporal distribution of each image product is similar around the explosion event; however, while the number of detections fall back down after the explosion for most of the image products, to the contrary, the difference images maintain a non-trivial count even after the explosion.

VI. CONCLUSIONS

VideoSAR circle-mode collections of the SPE-6 chemical explosion event were processed to create imagery, single polarization coherence, PolSAR coherence products, decomposition products, and Doppler smear detection. The fully-polarimetric VideoSAR continuous target interrogation allowed for high-precision coherent processing and polarimetric image product generation to monitor the surface change characteristics.

VideoSAR collection in a circular tragectory produces out-of-plane motion that violates the polar formatting assumptions for SAR image formation. Targets with height outside of a small depth of focus region, which were 1 meter or less for our collections, exhibit defocus. Therefore a digital elevation map-driven focusing algorithm was developed and applied to all imagery. The applied phase correction is identical on all channels of SAR data, because the underlying height values do not change.

Movies of time-varying, single polarization change products were generated. The integrating nature of the cross-track aperture requires a trade-off between cross-track resolution and time resolution, i.e., a shorter aperture. We present the full-resolution, two-dimensional products using an eight second aperture and low-resolution two-dimensional coherence products using a 0.5-second aperture that capture the dynamic change of the surface during the chemical explosion event. Dynamic coherence showed that the SPE pad surface scatterers moved in time, creating a permanent reduction in coherence. This decorrelated signal can be compared to seismic sensors and accelerometers to corroborate surface spallation. Fully-polarimetric coherence and maximum likelihood change detectors, showed that the ground around ground-zero and, to a lesser extent, an area in the northeastern direction from the experimental pad, decorrelated because of the explosion energy effecting the phase of scatterers within the region. Also, portions of the SPE pad lost coherence and then regained coherence. This phenomenon may be indicative of a transient elastic deformation during the explosion, or due to the Doppler energy injected into the scatterers in the scene from the explosion.

PolSAR change detection products were also produced. They showed more change occurred compared to a single polarization change detection. Compensating for thermal noise levels, a PolSAR change detection, similar to the single polarization MLCCD, was derived and applied to the SPE-6 explosion data. The noise compensated ML change corrected some of the decorrelation in the original Novak PolSAR change formulation. The final PolSAR change detection with noise correction still showed more change than single polarization. These results must be compared to others sensors to determine the final merit of the PolSAR approaches versus the single polarization results.

PolSAR movie products were also generated. Using the H/A/α polarimetric decomposition, the surface scattering mechanism near ground zero exhibits a migration from a Bragg scattering surface toward a random scattering surface during the explosion. This implies that the experiment pad scatterers were randomized, confirming what was also implied by the loss of coherence over the same area. Moreover, the H/A/α decomposition shows that the scattering mechanisms do not revert back to a Bragg scattering surface after the explosive energy has dissipated. This cannot be ascertained by only the coherence measures.

A detection algorithm that finds small Doppler smears in SAR imagery was applied to the

PolSAR imagery that were taken during the SPE-6 explosion. The Doppler detections on the bare earth were more readily detected with the HH, HV, and VH polarization channels as well as the HH-VV, HV+VH, and HV-VH coherent polarization channel combinations, while subtle movements in the rocky slope northeast of the experimental pad were more readily detected by the VV polarization channel as well as the HH+VV coherent polarization channel combination. The Doppler blurring lasted approximately 4.0 seconds; the explosive energy that traveled to the surface had dissipated after that time.

In all, we've shown the remote sensing capabilities of a fully-polarimetric SAR to monitor the surface scattering effects produced by an underground chemical explosion. Further research will explore how these results compare to signals and measures from other sensors deployed during the test.

VII. ACKNOWLEDGEMENTS

The authors wish to thank the National Nuclear Security Administration, Defense Nuclear Nonproliferation Research and Development, for sponsoring this work. We would also like to thank the Source Physic Experiment team, a multi-institutional and interdisciplinary group of scientists and engineers, for its technical contributions. Our thanks to Steve Vigil and Dylan Anderson from SNL who collected LIDAR height measures. Thanks to Dale Dubbert, Leroy Garley, Scott Devonshire, and the rest of the SNL FARAD SAR team for handling flight logistics and collecting the VideoSAR data for us. A special thanks to Sammy Bolin and his SNL ground-truth team that supported SPE VideoSAR on the ground.

Sandia National Laboratories is a multimission laboratory managed and operated by National Technology and Engineering Solutions of Sandia, LLC., a wholly owned subsidiary of Honeywell International, Inc., for the U.S. Department of Energy's National Nuclear Security Administration under contract DE-NA0003525.

VIII. FIGURES

A. *Figure Captions*

Figure 1: (a) Google Earth© image of the SPE pad and support roads from the year 2013 with north up. A hill increases in elevation to the left of the pad. There is a slight downward slope to the right of the pad. (b) Geomapped (north-up) VV-polarized full SAR image of the Source Physics Experiment site. The image has square pixels with 0.125-meter ground-plane resolution.

Figure 2: (a) Detected VideoSAR geo-mapped image of the SPE pad with global PGA autofocus applied; note the smearing of the scatterers on the left side of the pad. Illustration of a zoomed in portion of the globally focused PGA image (b) without digital elevation applied and (c) with digital elevation autofocus applied.

Figure 3: Geo-mapped (north up) VideoSAR imagery of the SPE pad (a) before the explosion, (b) during the explosion, and (c) after the explosion.

Figure 4: Geo-mapped VideoSAR CCD maps of the SPE pad (a) before, (b) during, and (c) after the explosion. VideoSAR captures the reflective coherent disruption caused by the explosion.

Figure 5: Geo-mapped VideoSAR low-resolution (2-m x 0.125-m) coherence products of the SPE pad, (a) before the explosion, (b) 0.1 seconds into the explosion, (c) 0.25 seconds after the explosion, and (d) 0.5 seconds after the explosion.

Figure 6: (a) Magnitude SAR imagery of SPE experimental pad with selected areas for monitoring coherence change. Blue - area near ground zero, Green - muck pond, Red - area approximately 100 meters from ground zero. (b) Plot of the coherence in each of the three areas described above as a function of time. The explosion occurred at $\sim$0.4 seconds. The integrating effect of the synthetic aperture causes an apparent lag in the event time.

Figure 7: Illustration of (a) traditional CCD and (b) MLCCD images before the explosion. The MLCCD approach removes low coherence due to low clutter-to-noise levels in the complex imagery.

Figure 8: Illustration of (a) traditional CCD and (b) MLCCD images after the explosion. Since the MLCCD removes non-changes, the low values in (b) are changes to the surface caused by the explosive energy.

Figure 9: Illustration of color-composite images of the $H/A/\alpha$ decomposition of the scene from passes (a) before, (b) during, and (c) after the explosion. There is a hue change on the pad between the pass before and the passes both with and after the explosion.

Figure 10: Plots of the contours that contain 50% of the 2-D histogram mass in the H/α plane. The blue contours are from the pass before the explosion for frames 1, 56, and 180. The red, orange, and yellow contours are from the pass with the explosion for: frame 1, before the explosion; frame 56, during the explosion; and frame 180, after the explosion, respectively. The remaining green contours are from the pass after the explosion for the same frame numbers. The blue dots, which cluster close together, show the H/α centroids for each of the 180 frames. The red dots, which start near the cluster of blue dots, migrate to higher entropy and α values as the explosion occurs and remain in a cluster for the remainder of the frames. The green dots are the centroids from a pass after the explosion; they remain at a higher entropy than the centroids before the explosion.

Figure 11: Plots of the area of the contours that contain 50% of the 2-D histogram mass in the H/α plane. The blue plot gives the area of the baseline pass and the red plot gives the area of the pass with the explosion. The green plot is from the pass after the explosion. It is clear that the explosion occurs around frame 40 and the peak response is around frame 56.

Figure 12: Illustration of optimum coherence (a) before the explosion and (b) after the explosion. The coherence is maximized between polarimetric channels giving the highest possible coherence.

Figure 13: Illustration of (a) Novak CCD and (b) Novak CCD with noise correction after the explosion.

Figure 14: Illustration of the centroids of the Doppler detection that were found in (a) the co-polarization channels (VV = red and HH = yellow) and (b) the cross-polarization channels (HV = red and VH = yellow). (Note, the centroid dots are overlaid on an exemplar SAR image from the VideoSAR collect. Some of the Doppler centroids detected in the other VideoSAR images may come from locations that are not in the exemplar SAR image. The dots from these centroids are placed at the edge of the image.)

Figure 15: Illustration of the Doppler detections that were found in the sum and difference of (a) the co-polarization channels (HH+VV = red and HH-VV = yellow) and (b) the cross-polarization channels (HV+VH = red and HV-VH = yellow). (Note, the centroid dots are overlaid on an exemplar SAR image from the VideoSAR collect. Some of the Doppler centroids detected in the other VideoSAR images may come from locations that are not in the exemplar SAR image. The dots from these centroids are placed at the edge of the image.)

Figure 16: Illustration of the number of Doppler detections that were found in each frame for the different image products from the PolSAR image sets.

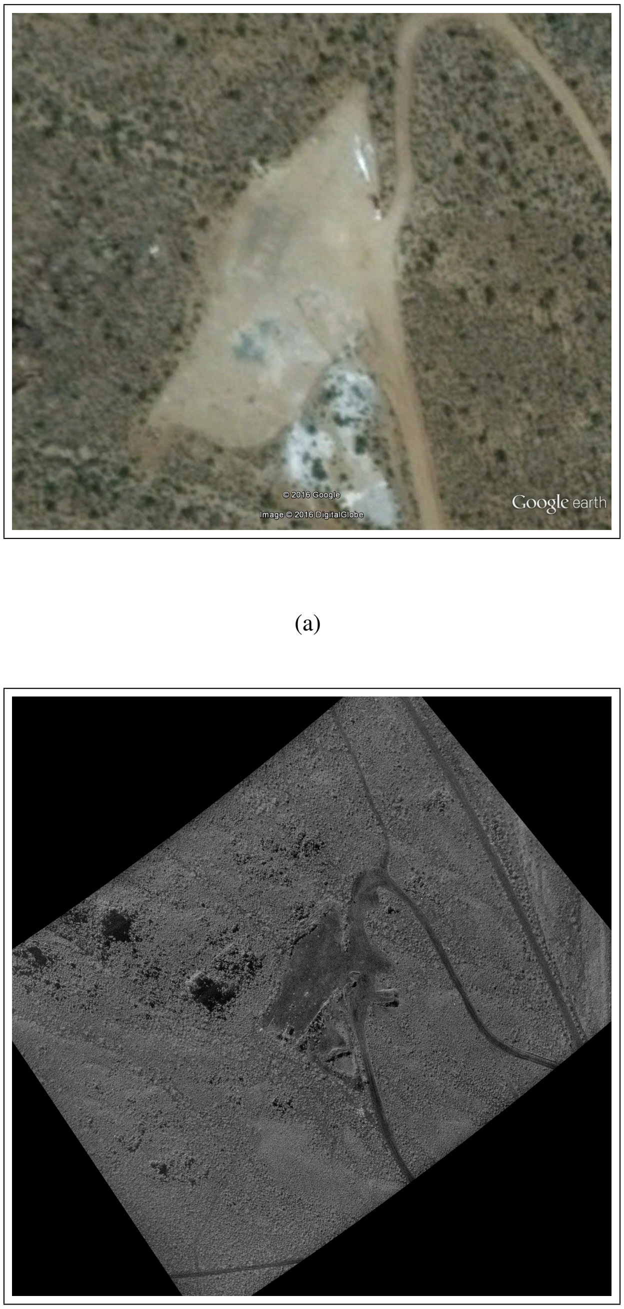

(a)

(b)

Fig. 1.

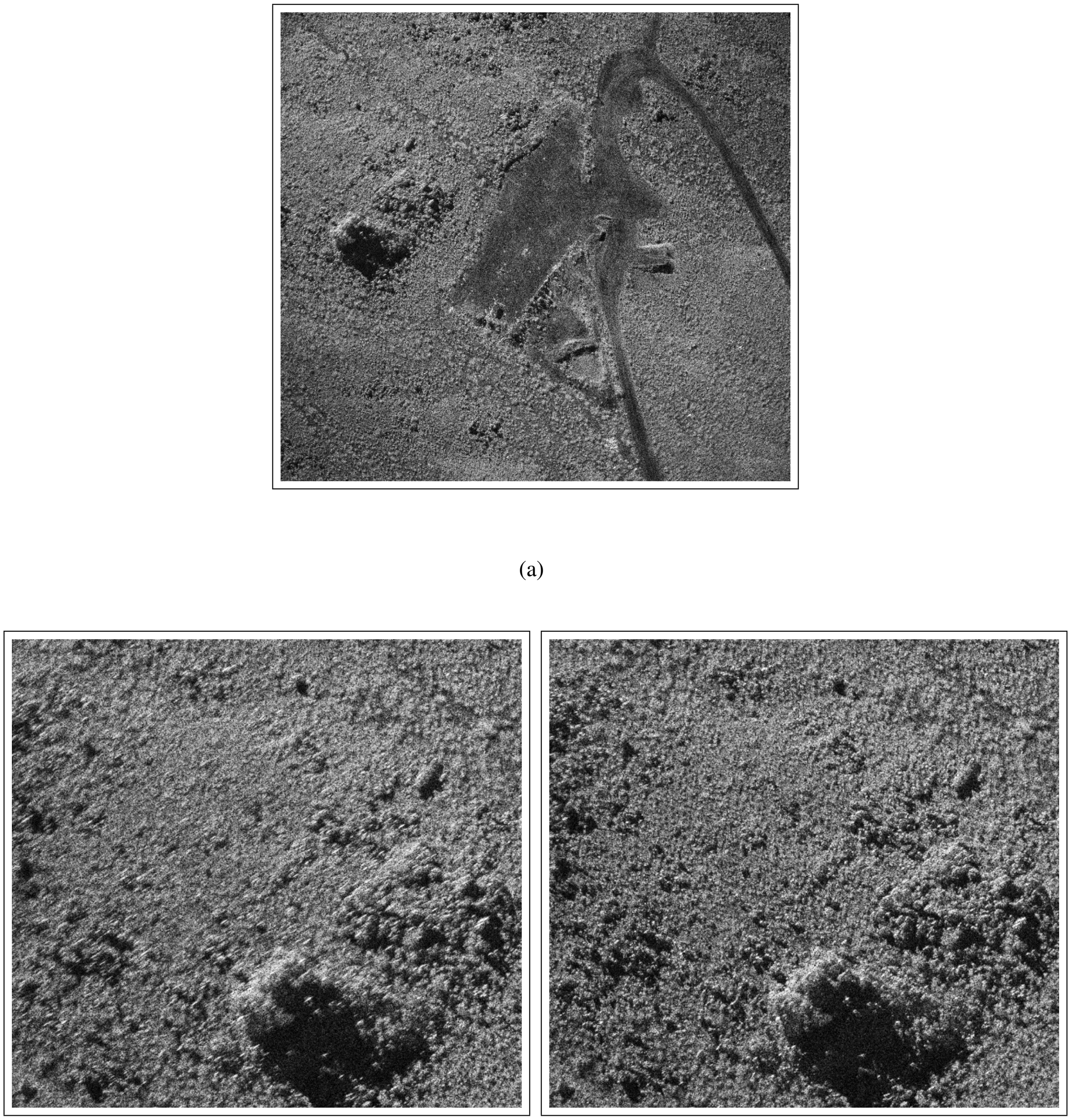

(a)

(b)

(c)

Fig. 2.

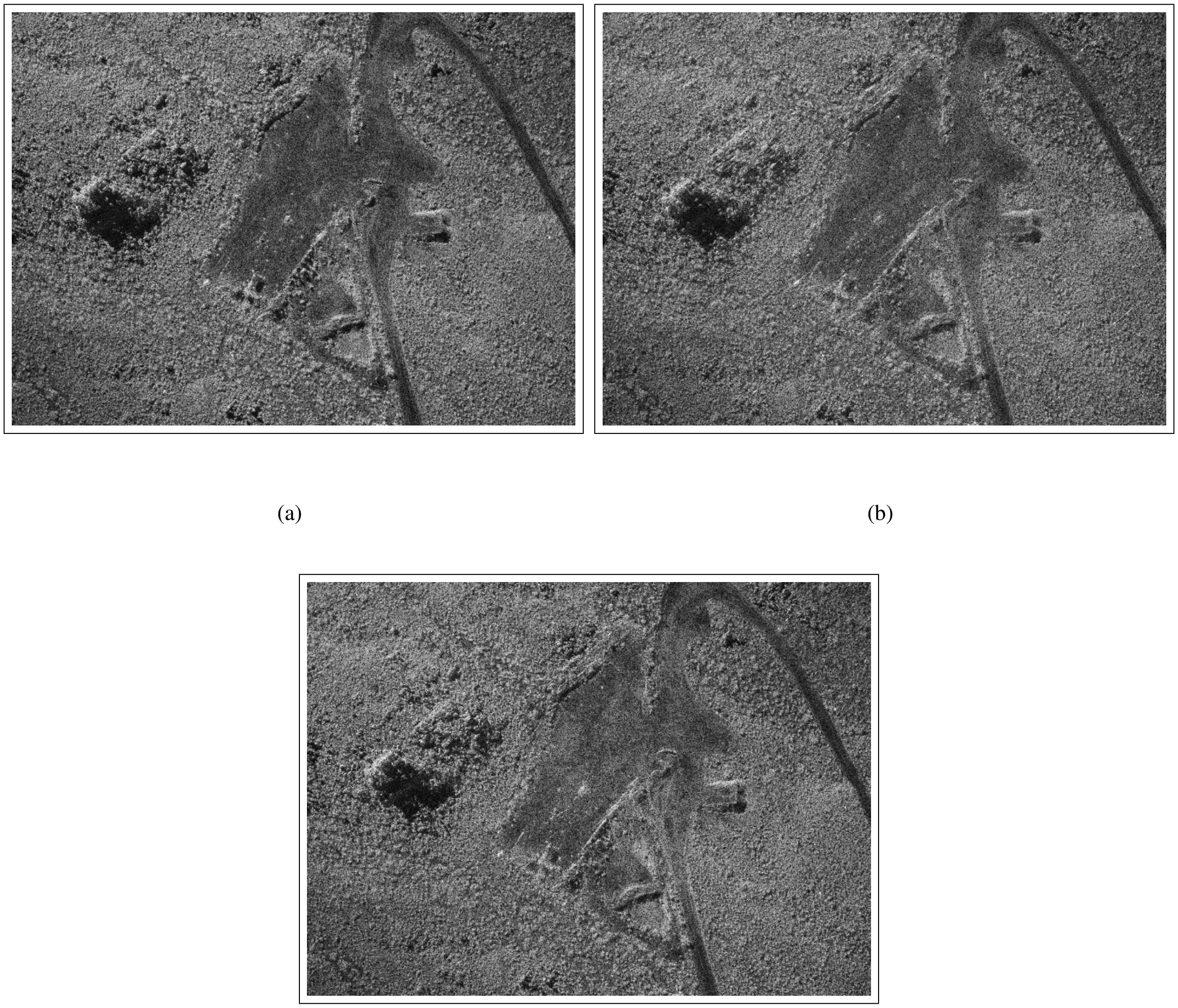

(a)

(b)

(c)

Fig. 3.

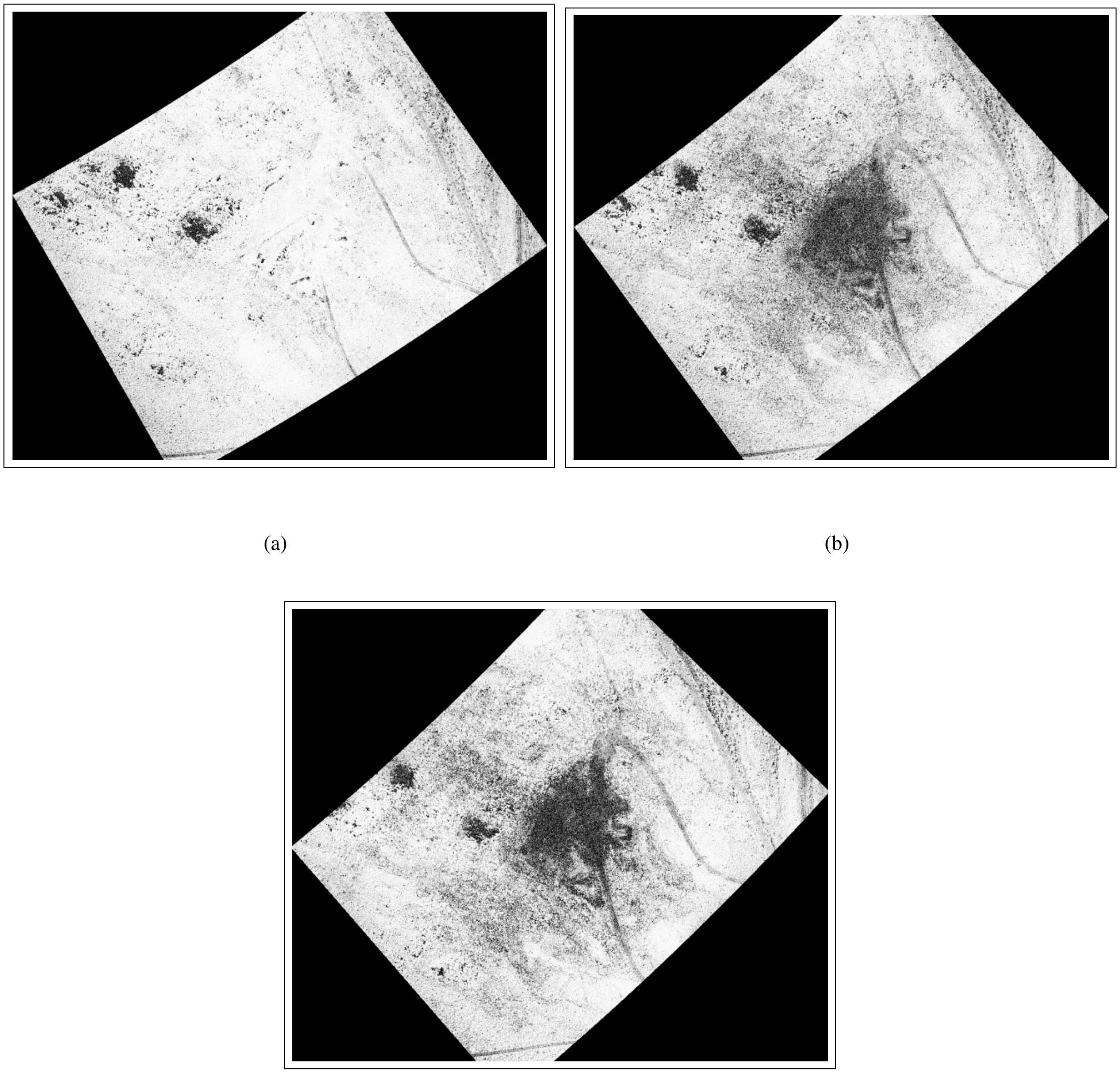

(a)

(b)

(c)

Fig. 4.

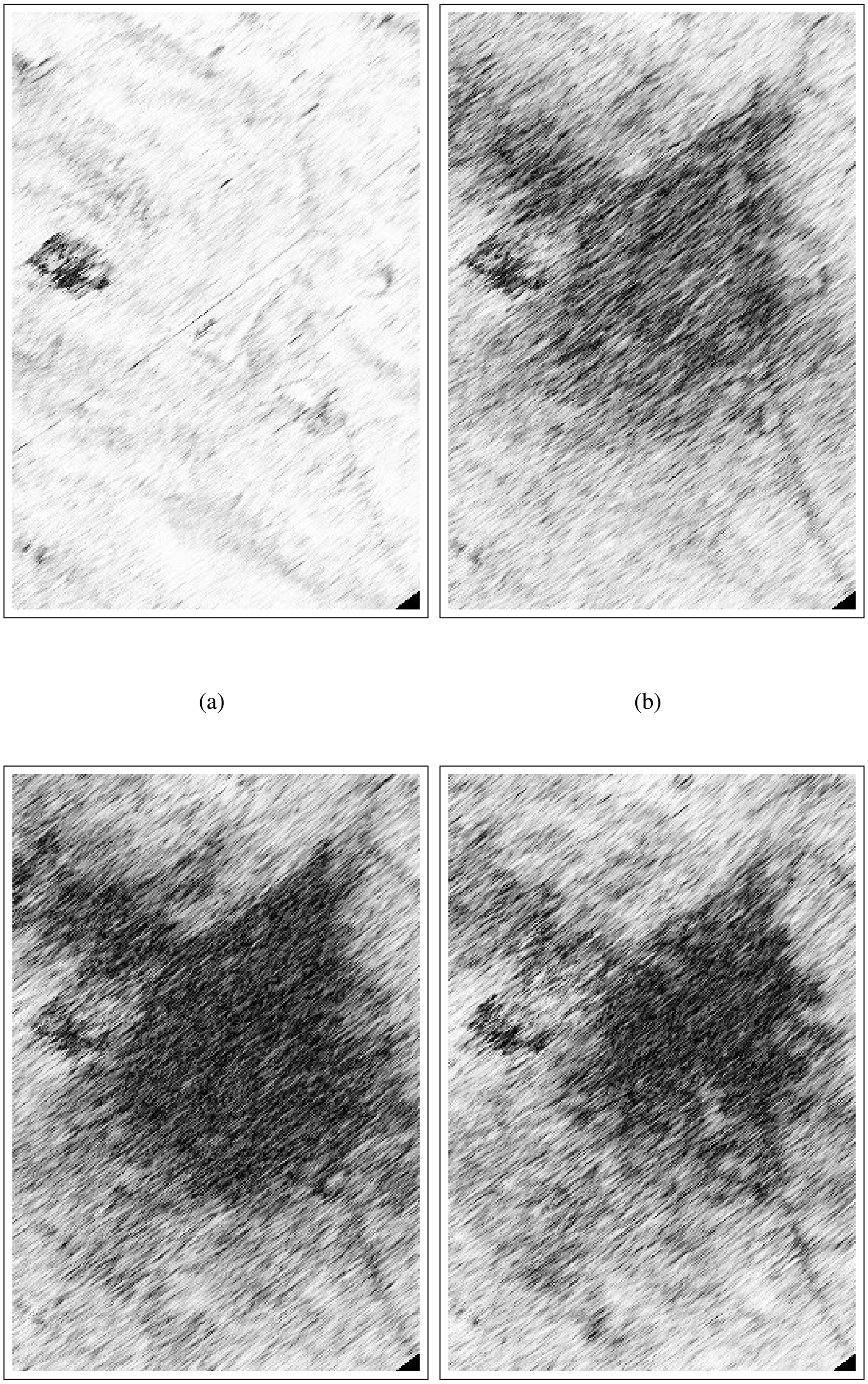

(a) (b)

(c) (d)

Fig. 5.

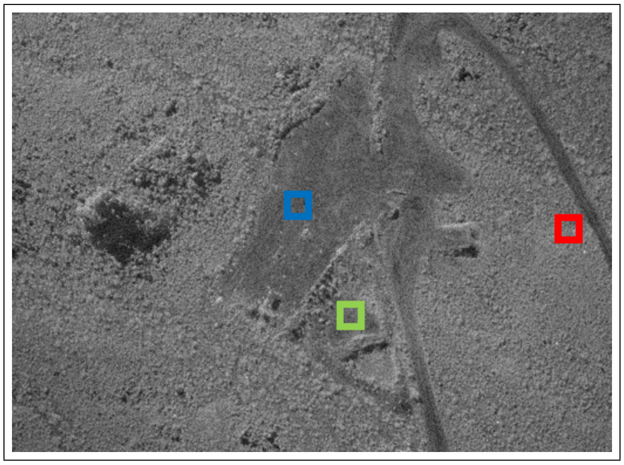

(a)

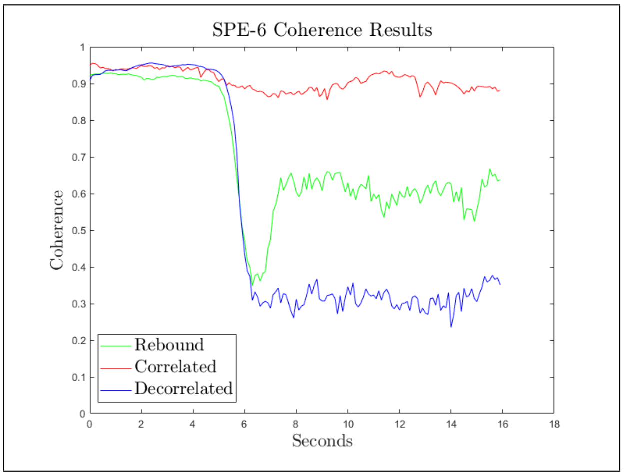
SPE-6 Coherence Results
Coherence
Seconds
0
0.1
0.2
0.3
0.4
0.5
0.6
0.7
0.8
0.9
1
0
2
4
6
8
10
12
14
16
18
Rebound
Correlated
Decorrelated

(b)

Fig. 6.

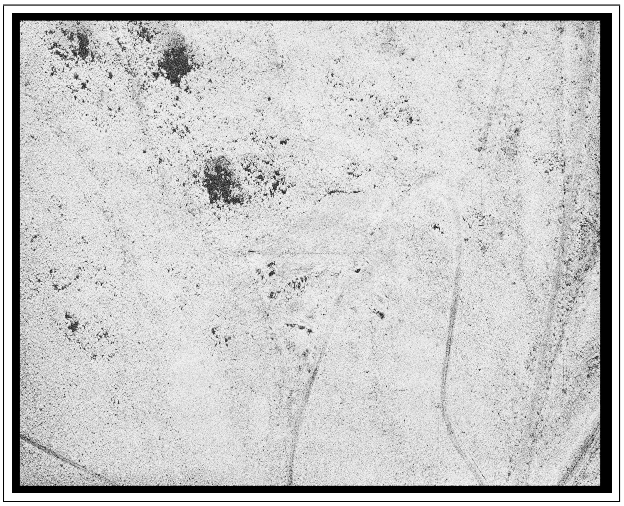

(a)

(b)

Fig. 7.

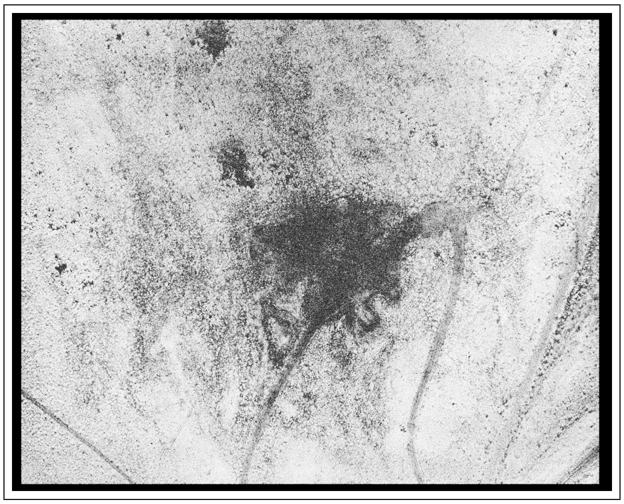

(a)

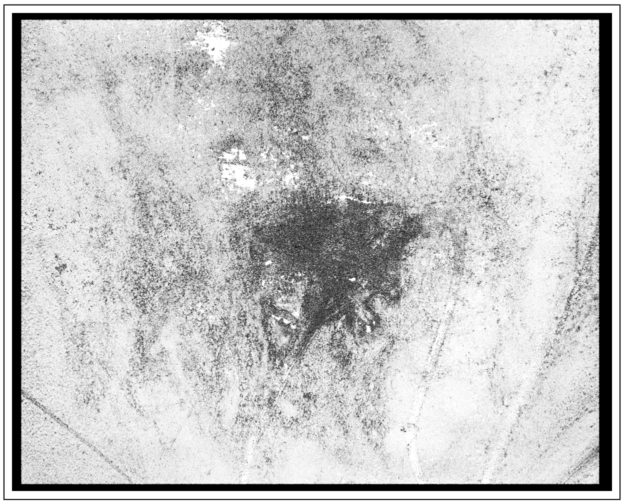

(b)

Fig. 8.

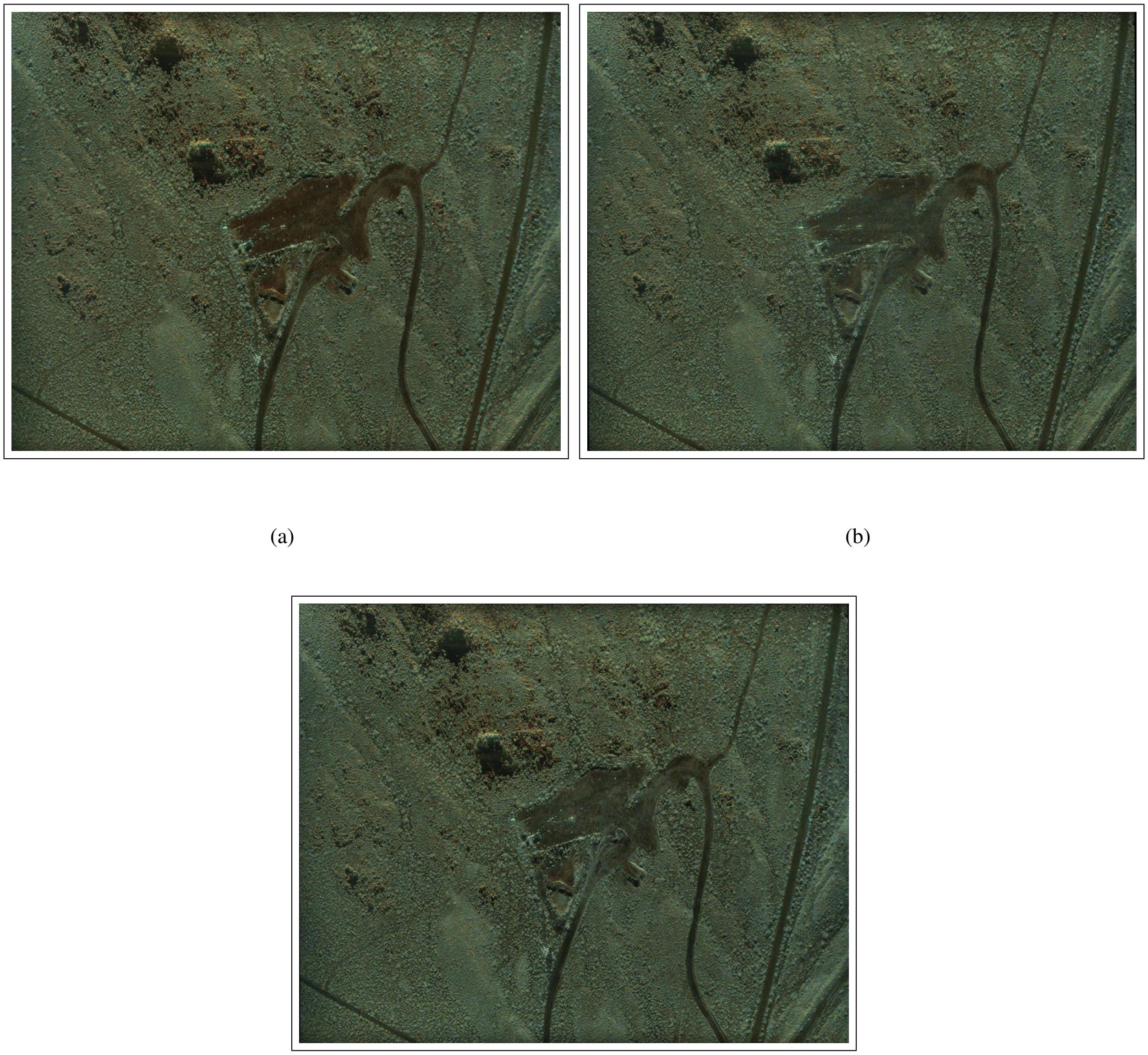

(a)

(b)

(c)

Fig. 9.

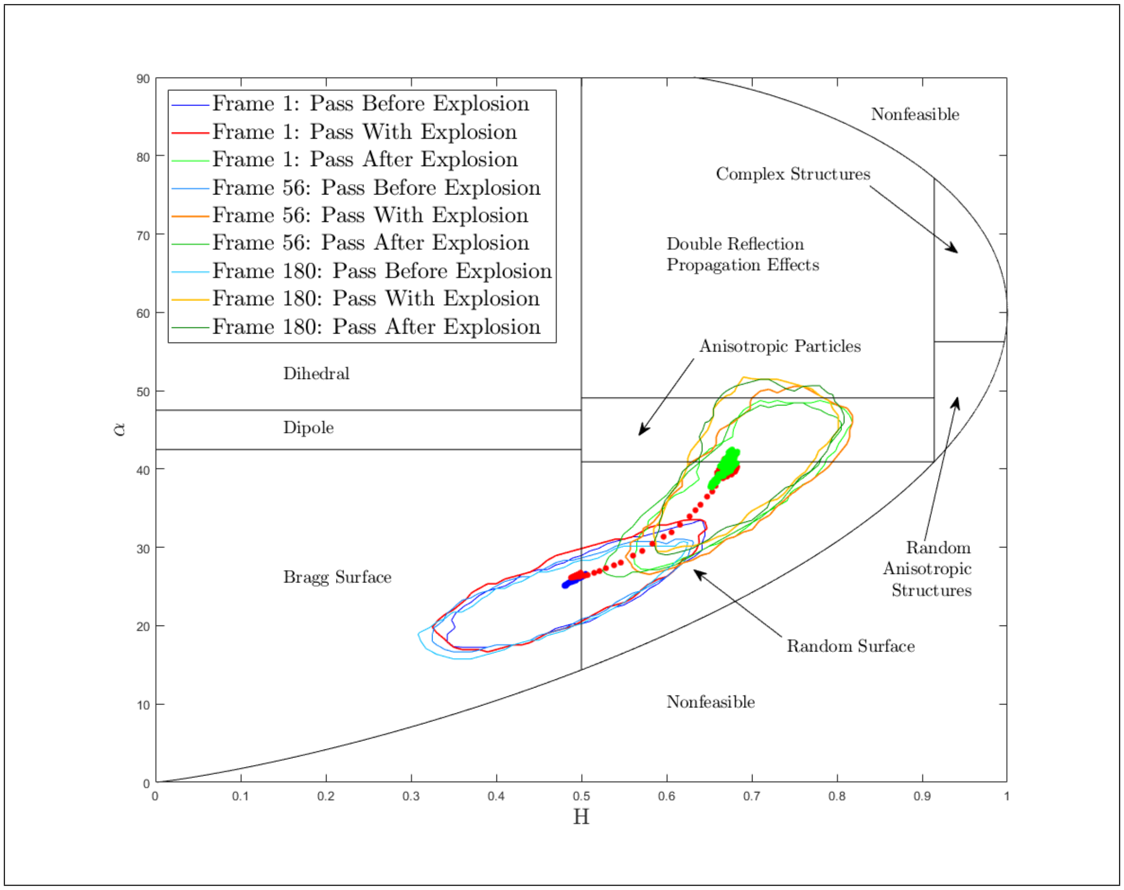
Frame 1: Pass Before Explosion
Frame 1: Pass With Explosion
Frame 1: Pass After Explosion
Frame 56: Pass Before Explosion
Frame 56: Pass With Explosion
Frame 56: Pass After Explosion
Frame 180: Pass Before Explosion
Frame 180: Pass With Explosion
Frame 180: Pass After Explosion
Nonfeasible
Complex Structures
Double Reflection
Propagation Effects
Anisotropic Particles
Dihedral
Dipole
Bragg Surface
Random Surface
Random
Anisotropic
Structures
Nonfeasible
α
H
0
10
20
30
40
50
60
70
80
90
0
0.1
0.2
0.3
0.4
0.5
0.6
0.7
0.8
0.9
1

Fig. 10.

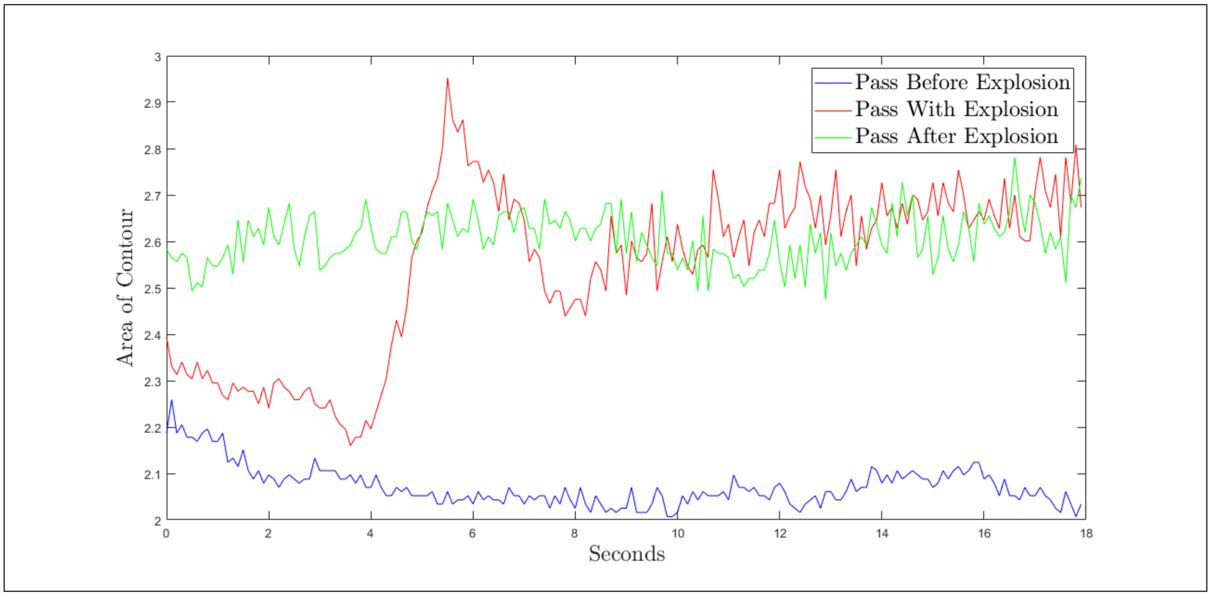
3
2.9
2.8
2.7
2.6
2.5
2.4
2.3
2.2
2.1
2
0
2
4
6
8
10
12
14
16
18
Area of Contour
Seconds
Pass Before Explosion
Pass With Explosion
Pass After Explosion

Fig. 11.

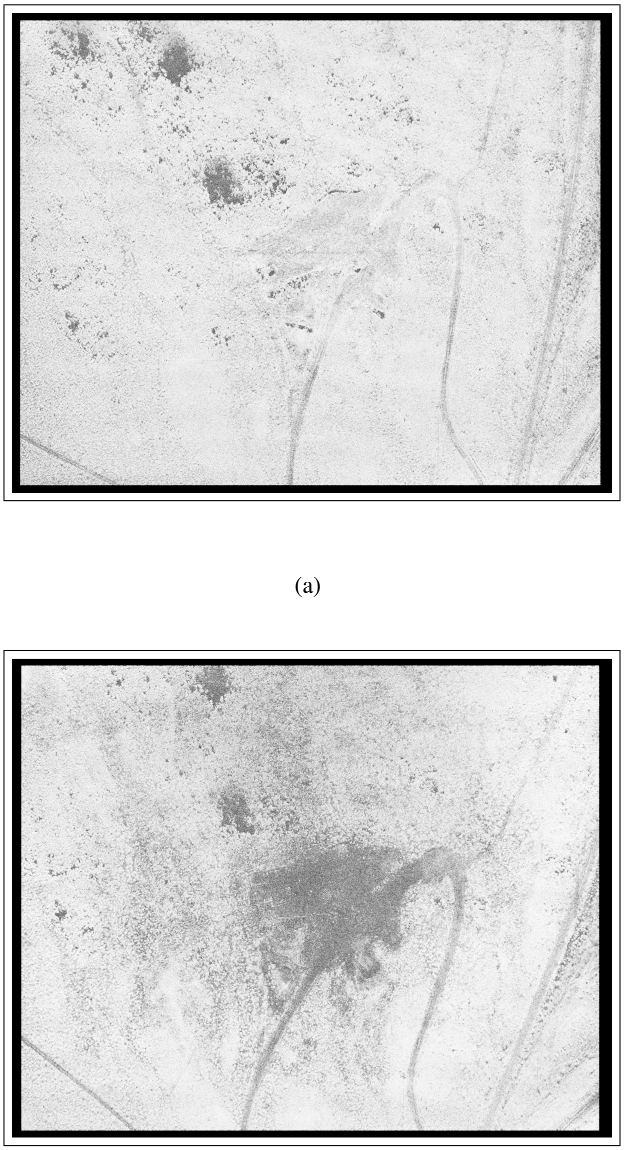

(a)

(b)

Fig. 12.

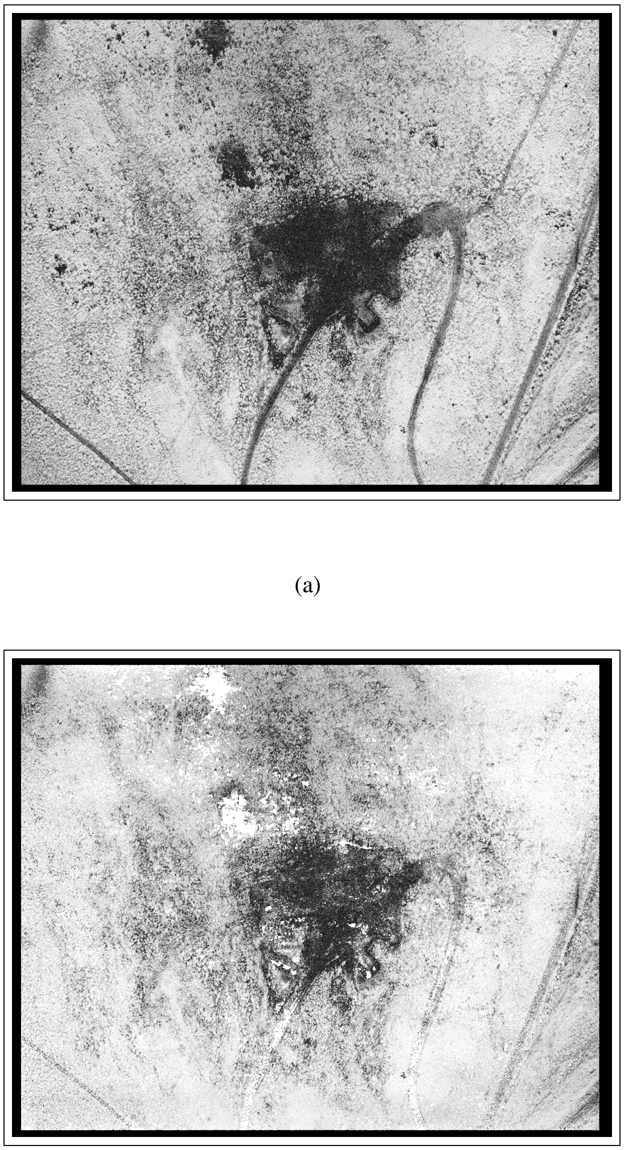

(a)

(b)

Fig. 13.

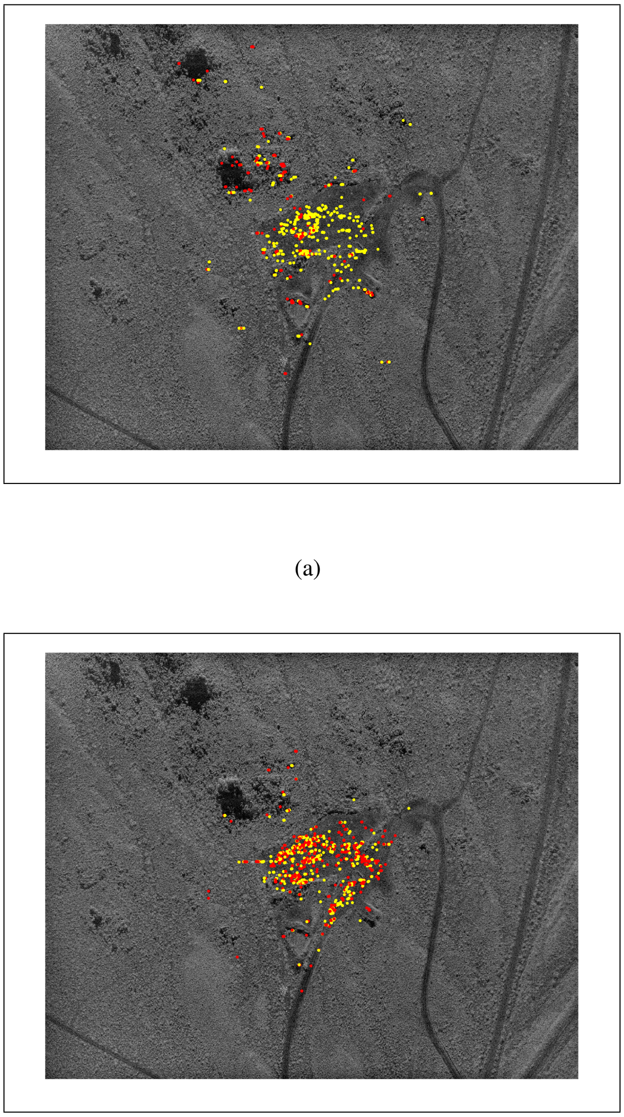

(a)

(b)

Fig. 14.

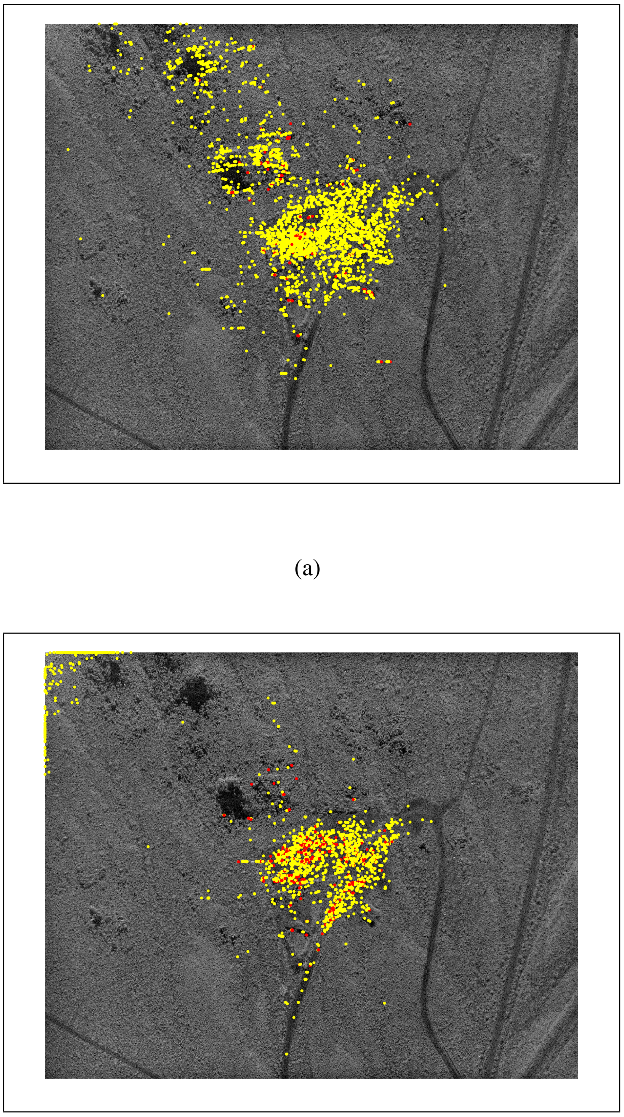

(a)

(b)

Fig. 15.

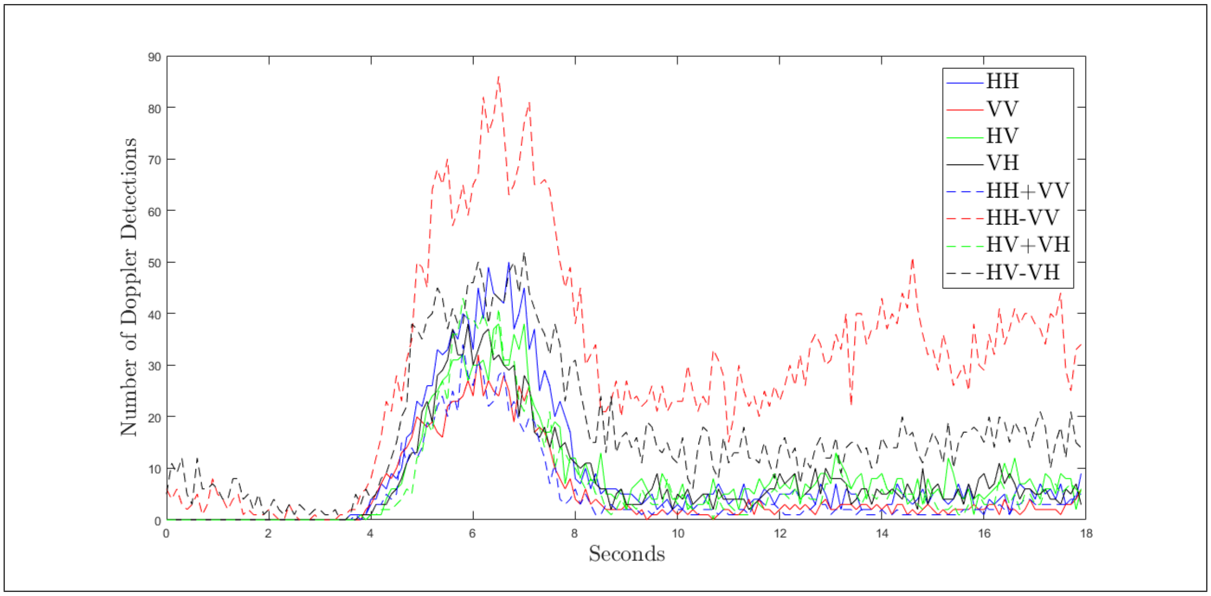
Number of Doppler Detections
Seconds
0
10
20
30
40
50
60
70
80
90
0
2
4
6
8
10
12
14
16
18
HH
VV
HV
VH
HH+VV
HH-VV
HV+VH
HV-VH

Fig. 16.

REFERENCES

[1] C. M. Snelson, R. E. Abbott, S. T. Broome, R. J. Mellors, H. J. Patton, A. J. Sussman, M. J. Townsend, and W. R. Walter, “Chemical explosion experiments to improve nuclear test monitoring,” *Eos, Transactions of the American Geophysical Union*, vol. 94, no. 27, pp. 237–239, 2013.

[2] C. V. Jakowatz, Jr., D. E. Wahl, P. E. Eichel, D. C. Ghiglia, and P. A. Thompson, *Spotlight-Mode Synthetic Aperture Radar: A Signal Processing Approach*. Kluwer Academic Publishers, 1996.

[3] L. Wells, K. Sorensen, A. Doerry, and B. Remund, “Developments in SAR and IfSAR systems and technologies at Sandia National Laboratories,” in *2003 IEEE Aerospace Conference Proceedings*, vol. 2, March 2003.

[4] P. H. Eichel, “The direction cosine method of scatterer location extended to spotlight-mode IfSAR,” in *Conference Record of the Thirty-Fourth Asilomar Conference on Signals, Systems and Computers*, vol. 1, Oct 2000, pp. 21–24.

[5] D. A. Yocky, T. M. Calloway, and D. E. Wahl, “VideoSAR collections to image underground chemical explosion surface phenomology,” in *Proceedings of the SPIE, Radar Sensor Technology XXI*, vol. 10188, April 2017.

[6] D. E. Wahl, P. H. Eichel, D. C. Ghiglia, and C. V. Jakowatz, “Phase gradient autofocus-a robust tool for high resolution SAR phase correction,” *IEEE Transactions on Aerospace and Electronic Systems*, vol. 30, no. 3, pp. 827–835, Jul 1994.

[7] M. Born and E. Wolf, *Principles of Optics, Sixth Edition*. Pergamon Press, 1980.

[8] E. Rodriguez and J. M. Martin, “Theory and design of interferometric synthetic aperture radars,” *IEE Proceedings F - Radar and Signal Processing*, vol. 139, no. 2, pp. 147–159, April 1992.

[9] L. C. Graham, “Synthetic interferometer radar for topographic mapping,” *Proceedings of the IEEE*, vol. 62, no. 6, pp. 763–768, June 1974.

[10] H. A. Zebker and R. M. Goldstein, “Journal of geophysical research,” *Topographic mapping from interferometric synthetic aperture radar observations*, vol. 91, no. B5, pp. 4993–4999, 1986.

[11] A. L. Gray and P. J. Farris-Manning, “Repeat-pass interferometry with airborne synthetic aperture radar,” *IEEE Transactions on Geoscience and Remote Sensing*, vol. 31, no. 1, pp. 180–191, Jan 1993.

[12] D. Massonnet, M. Rossi, C. Carmona, F. Adragna, G. Peltzer, K. Feigl, and T. Rabaute, “The displacement field of the landers earthquake mapped by radar interferometry,” *Nature*, vol. 364, no. 6433, pp. 138–142, 1993.

[13] A. Ferretti, C. Prati, and F. Rocca, “Permanent scatterers in SAR interferometry,” *IEEE Transactions on Geoscience and Remote Sensing*, vol. 39, no. 1, pp. 8–20, Jan 2001.

[14] D. E. Wahl, D. A. Yocky, C. V. Jakowatz, and K. M. Simonson, “A new maximum-likelihood change estimator for

two-pass SAR coherent change detection," *IEEE Transactions on Geoscience and Remote Sensing*, vol. 54, no. 4, pp. 2460–2469, April 2016.

[15] J. Lee and E. Pottier, *Polarimetric Radar Imaging: From Basics to Applications*. CRC Press, 2002.

[16] G. Singh, Y. Yamaguchi, and S. E. Park, "General four-component scattering power decomposition with unitary transformation of coherency matrix," *IEEE Transactions on Geoscience and Remote Sensing*, vol. 51, no. 5, pp. 3014–3022, May 2013.

[17] S. Dauphin, "General model-based decomposition framework for polarimetric SAR images," Ph.D. dissertation, Dept. Math, Colorado State University, 2017.

[18] S. R. Cloude and E. Pottier, "An entropy based classification scheme for land applications of polarimetric SAR," *IEEE Transactions on Geoscience and Remote Sensing*, vol. 35, no. 1, pp. 68–78, Jan 1997.

[19] S. R. Cloude and K. P. Papathanassiou, "Polarimetric SAR interferometry," *IEEE Transactions on Geoscience and Remote Sensing*, vol. 36, no. 5, pp. 1551–1565, Sep 1998.

[20] L. M. Novak, "Coherent change detection for multi-polarization SAR," in *Conference Record of the Thirty-Ninth Asilomar Conference on Signals, Systems and Computers, 2005.*, Oct 2005, pp. 568–573.

[21] R. K. Raney, "Synthetic aperture imaging radar and moving targets," *IEEE Transactions on Aerospace and Electronic Systems*, vol. 7, no. 3, pp. 499–505, Mar 1971.

[22] V. C. Chen, F. Li, S. Ho, and H. Wechsler, "Micro-doppler effect in radar: Phenomenon, model, and simulation study," *IEEE Transactions on Aerospace and Electronic Systems*, vol. 42, no. 1, pp. 2–21, Jan 2006.